[9]J. H. Miller and H. P. Kelly, Phys. Rev. (to be published).

[10]O. Sinanoglu and I. Öksüz, Phys. Rev. Letters 21, 507 (1968).

[11]R. K. Nesbet, Phys. Rev. 175, 2 (1968).

[12]J. W. Viers, F. E. Harris, and H. F. Schaefer III, Phys. Rev. A 1, 24 (1970).

[13]T. L. Barr and E. R. Davidson, Phys. Rev. A 1,

644 (1970).

[14]C. F. Bunge and E. M. A. Peixoto, Phys. Rev. A 1, 1277 (1970).

[15]A. Bunge and C. F. Bunge, Phys. Rev. A 1, 1599 (1970).

[16]E. Clementi, IBM J. Res. Develop. 9, 2 (1965).

[17]E. J. Kansa (unpublished).

[18]H. P. Kelly, Phys. Rev. 134, A1450 (1964).

Lamb Shift in Singly Ionized Helium[†]

Musti A. Narasimham

IBM Components Division, East Fishkill Facility, Hopewell Junction, New York 12533

and

Richard L. Strombotne[*]

Office of the Secretary, U. S. Department of Transportation, Washington D. C. 20591

(Received 31 July 1970)

The energy separation S between the $2\,^2S_{1/2}$ and $2\,^2P_{1/2}$ states of singly ionized helium was measured using a microwave method. Helium atoms in the space between the plates of a spherical-mirror Fabry-Perot resonator are bombarded continuously by electrons of 200-eV energy to produce helium ions in the $2\,^2S_{1/2}$ metastable state. The applied modulated rf power induces transitions in the metastable ions to the short-lived $2\,^2P_{1/2}$ state. The 40.8-eV photons emitted by the decay of the $2\,^2P_{1/2}$ ions to the ionic ground state $1\,^2S_{1/2}$ are quantum converted to visible photons by a scintillator and are then guided to a photomultiplier. The output of the photomultiplier is detected and amplified synchronously with the rf power. The experiment made use of the Zeeman effect of the fine structure and is performed in an applied homogeneous magnetic field. Three different operating values for the helium pressure are used and the result is extrapolated to a zero-pressure value. A thorough search was made for all possible systematic errors in the experiment. The value for S thus obtained is 14 046.2 ± 2.0 MHz. The quoted uncertainty consists of three standard deviations for the statistical error plus estimates of systematic errors. This result agrees with the previous experimental values for S (within three standard deviations), and with the latest theoretical value of 14 044.5 ± 5.2 MHz.

I. INTRODUCTION

The fine structure of the $n = 2$ level of hydrogen and deuterium has been studied by Lamb and his collaborators,[1] using an atomic-beam rf power method. Their experiments established the existence of a small energy separation between the $2\,^2S_{1/2}$ and $2\,^2P_{1/2}$ levels of these atoms, which are degenerate according to the Dirac theory, and also gave precise values for these separations. This separation, the Lamb shift, is a result of the interaction of the atomic electron with its own (virtual) radiation field; thus, purely of radiative origin, it provided a test for the validity of the theory of quantum electrodynamics. Measurements of the Lamb shift in hydrogen by Robiscoe[2] and deuterium by Cosens[3] have been made using a level-crossing technique with results of precision equal to those of Lamb.

The Lamb shift in the $n = 2$ level of singly ionized helium has been measured by Lamb and Skinner[4];

Yergin[5]; Novick, Lipworth, and Yergin[6]; and Lipworth and Novick.[7] The values they measured for S are 14 020 ± 100, 14 021 ± 60, 14 043 ± 13, and 14 040.2 ± 4.5 MHz, respectively.

The work reported here is directed towards precision remeasurement of the Lamb shift S in the $n = 2$ level of singly ionized helium. Radio frequency power was used to induce the Lamb-shift transition. A phase-sensitive detection scheme was used for the signal measurements. Considerable effort was made to keep the apparatus stable during the period of an experimental run, and a procedure that provides a check on the stability of the system in each run was employed to obtain precision resonance data. Much of the data was collected under different operating characteristics of the apparatus, and a thorough search was made for possible systematic corrections to the final result.

Section II describes the experimental method, Sec. III discusses the details of the apparatus, and Sec. IV includes the operating characteristics of
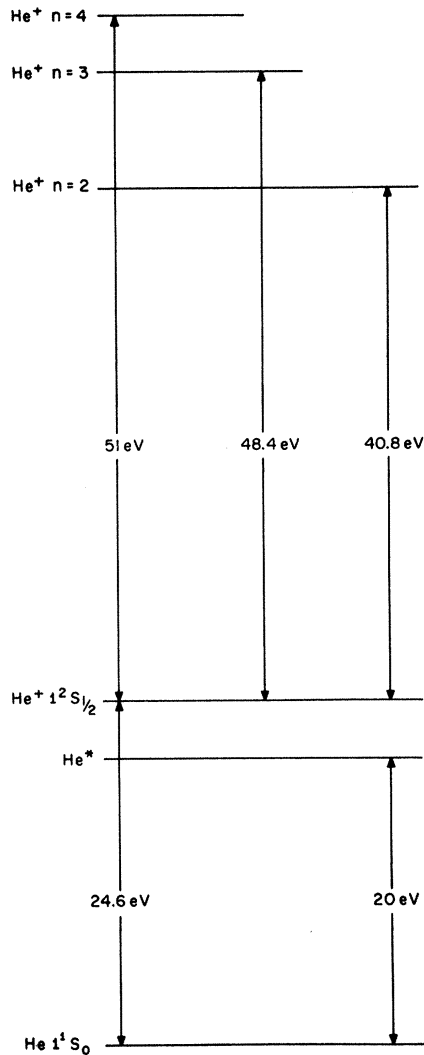
FIG. 1. Energy levels of He and He$^+$ (note that the He$^+$ levels are not complete).

the apparatus. The various ion-removal processes that have an influence on the ion-removal time are discussed in Sec. V which also includes a description of the observed resonance line shape. The procedure used to collect precision resonance data is described in Sec. VI and all possible corrections and uncertainties to the final result are discussed in Sec. VII. Section VIII presents the final result with related discussion.

II. EXPERIMENTAL METHOD

The $2\,^2S_{1/2}$ state of singly ionized helium is metastable because the dipole transitions to the ionic ground state $1\,^2S_{1/2}$ are forbidden by $\Delta l \neq \pm 1$. The natural lifetime of this metastable state is about 2 msec in the absence of external electromagnetic fields.[8] However, the ionic state $2\,^2P_{1/2}$ is short

lived with a natural lifetime of 10^{-10} sec; hence, ions in this state decay to the ionic ground state in 10^{-10} sec. In doing so, these ions emit photons of wavelength appropriate to the $2\,^2P_{1/2}$-$1\,^2S_{1/2}$ energy separation, which is about 304 Å. The rf power at the appropriate frequency induces transitions in the ions that exist in the $2\,^2S_{1/2}$ metastable state to the short-lived $2\,^2P_{1/2}$ state, which will then decay to the ionic ground state. This additional flux of 304-Å photons constitutes the signal and by sweeping the rf frequency, it is possible to obtain the resonance line shape and locate the resonance line center. This precision measurement was made in an applied homogeneous magnetic field keeping the frequency of the rf power constant and the magnetic field was swept to obtain the resonance line.

Helium gas contained in the space between the two reflecting mirrors of a spherical Fabry-Perot resonator is bombarded continuously with electrons accelerated through 200 V. A small fraction of the bombarded atoms is ionized and excited to the $2\,^2S_{1/2}$ metastable state of interest, constituting about 1% (estimated) of the ion content. In addition, ions and atoms exist in other excited states. The relevant energy-level diagram for the He atom and He$^+$ ion (up to $n = 4$ of the ion and excluding the fine structure) is shown in Fig. 1. Figure 2 shows the fine structure of the $n = 2$ level of the ion. In an external magnetic field, the $2\,^2S_{1/2}$ and $2\,^2P_{1/2}$ states split into the magnetic substances α, β and e, f, respectively, as shown in Fig. 3. The $\alpha \rightarrow e$ transition was chosen for study and the selected rf frequency was such that $\alpha \rightarrow e$ resonance peak occurs at a magnetic field close to the βf crossing field, for reasons discussed in Sec. VII A d. Microwave power is fed into the resonator with the electric field vector parallel to the applied magnetic field since the $\alpha \rightarrow e$ transition is a $\pi(\Delta m = 0)$ transition.

The rf field induces a transition from the α state to the e state. Ions thus transferred decay rapidly to the ionic ground state (to magnetic substates α', β' of the ground state $1\,^2S_{1/2}$) emitting 304-Å photons. The uv photons that escape into the direction of the light pipe pass through an aluminum
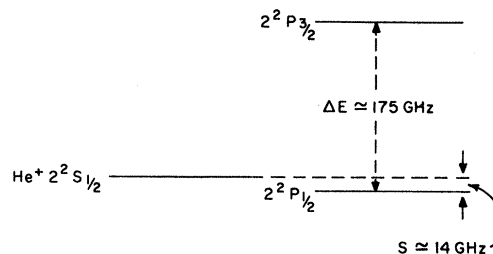

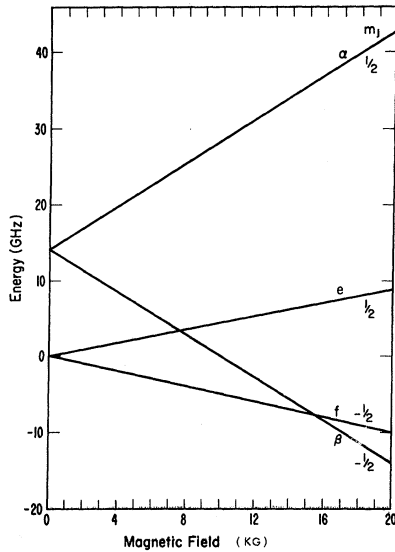FIG. 2. Fine structure of singly ionized helium, $n = 2$ level.

FIG. 3. Zeeman effect of the $2\,^2S_{1/2}$ and $2\,^2P_{1/2}$ states. α, β and e, f are the magnetic substates of $S_{1/2}$ and $P_{1/2}$ states.

filter and strike a sodium salicylate scintillator, where they are quantum-converted. Part of the visible light thus produced is collected by a light pipe and guided to a photodetector.

The rf induced signal forms a small addition to a large background (typically 0.3%). The background comes from the deexcitation radiation of the short-lived excited ionic states, atomic states, and leakage of the visible light from the filament that provides the electron bombarding current. Hence, a lock-in detection method is used to detect the resonance signal. A schematic arrangement of the modulation and detection apparatus is shown in Fig. 4. The rf power is modulated by a ferrite modulator at a rate of 50 Hz and the resonance signal is detected synchronously by a phase-sensitive detector-amplifier. The total background is continuously monitored by a vacuum tube voltmeter (VTVM). The oe-transition resonance signal strength was measured as a function of the magnetic field from which the resonance line center corresponding to the applied rf frequency was determined. The Zeeman transition frequency as a function of the magnetic field is shown in Fig. 5. By making use of the theory of Zeeman effect,[9] the resonance line center measured in the magnetic field space was interpolated to yield the zero-field Lamb-shift value s.

III. APPARATUS

The experimental setup is shown in Fig. 6. Attached to the rectangular-shaped vacuum box there are three long arms, the top one for the input of helium gas, the central one leading to the cold traps

and vacuum pumps, and the bottom one to the detector. A rectangular flange fits at the top of the vacuum box and supports the microwave apparatus and the electrode structure. Vacuum as good as 3×10^{-4} mTorr was obtained above the cold trap.

A. Interaction Space

The interaction of the α-state metastable ion with the rf field leads to the oe transition, which at a transition frequency close to 29 300 MHz is of interest in this experiment. This interaction occurs in the space between the plates of a spherical-mirror Fabry-Perot resonator designed to operate in this frequency range. The rf power is coupled into the resonator through a single iris with the appropriate polarization. The coupling-iris size was chosen to approximately maximize the microwave electric field with the resonator containing eight half-wavelengths. The rf quenching region is essentially defined by the ion-beam thickness (filament diameter plus ion cyclotron radius) and the spot size of the rf power ($\simeq 1.24$ cm). The bottom resonator plate is held rigid, while the top plate can be adjusted for resonance by a differential screw.

B. Electrode Structure

A beam of electrons at 200 eV bombarded the helium atoms to produce the metastable ions. The electron-beam source is a thoriated tungsten wire filament of 0.25-mm diam and approximately 19 mm long. As shown in Fig. 7, the filament is supported
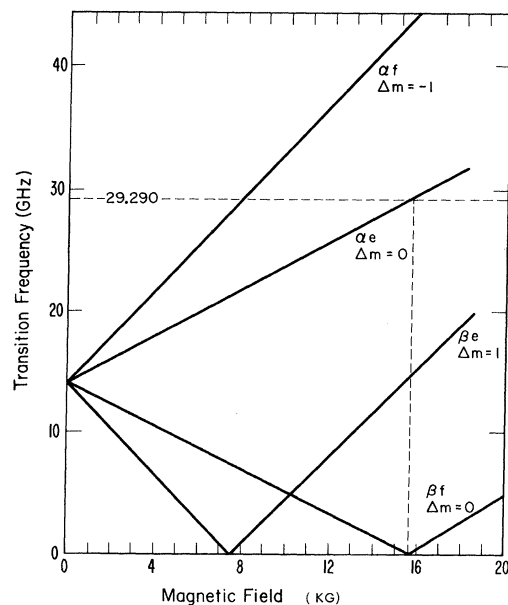

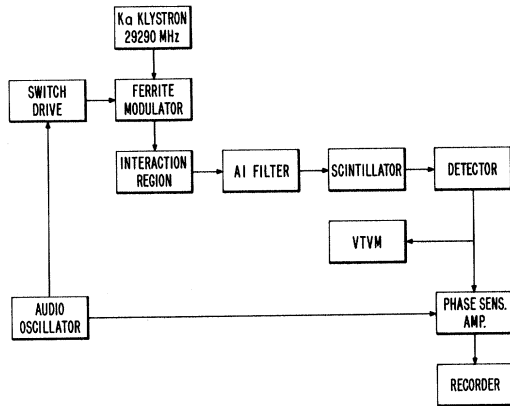FIG. 4. Block diagram of the experimental method.

FIG. 5. Zeeman transition frequencies as function of magnetic field.

under tension ($\simeq$ 4 lb) by molybdenum rods in such a way that the area of the current loop ($\simeq$ 25.0 mm^2) is small. The tension reduces the lateral displacement of the filament by the magnetic field. The filament is held 200 V negative with respect to the grounded acceleration grid GI which is 97% transparent to the electron beam. (Note that GI is between F and the interaction space.) The total emission current is servo-controlled to a constant value. Most of the emission current goes in the forward direction due to the presence of a strong magnetic field and since the electron reflector R is connected to the negative terminal of the filament power supply. After traveling across the interaction space (quenching region), the primary electron beam is collected by

the grounded anode screen grid GII (82% transparent) and anode A. The anode is maintained 45 V positive with respect to ground, so that secondary electrons produced at the anode do not reenter the interaction region. To give a 4.4-mA-beam current in the forward direction, the filament required a dc heating current of about 6.3 A.

C. Radio-Frequency Apparatus

The rf system is shown in Fig. 8. The rf power required to induce the αe transition, at a transition frequency of 29 290 MHz, is provided by a Ka-band klystron (K_1). The power passes through a variable attenuator (V_1), a power modulator (M), and is fed to the Fabry-Perot resonator (R).

Frequency stabilization of the rf source is achieved by a double phase-lock loop technique. In the first loop a Ku-band klystron (K_2) delivering 14 640-MHz radiation is phase locked with the reference frequency of 14 670 MHz. The second harmonic of 14 640 MHz is used as a reference to phase lock the Ku-band klystron. The manner in which the reference frequency 14 670 MHz is obtained from the 5-MHz NBS secondary-standard source is shown in Fig. 8. The frequency stability of the rf source is as good as the stability of the 5-MHz standard (few parts in 10^{11}), which is more than needed, since only a few parts in 10^7 are required for stability.

It is essential to keep the rf power level in the interaction space constant during the period of a run. To make relative power measurements, 1% of the power reflected by the resonator is withdrawn
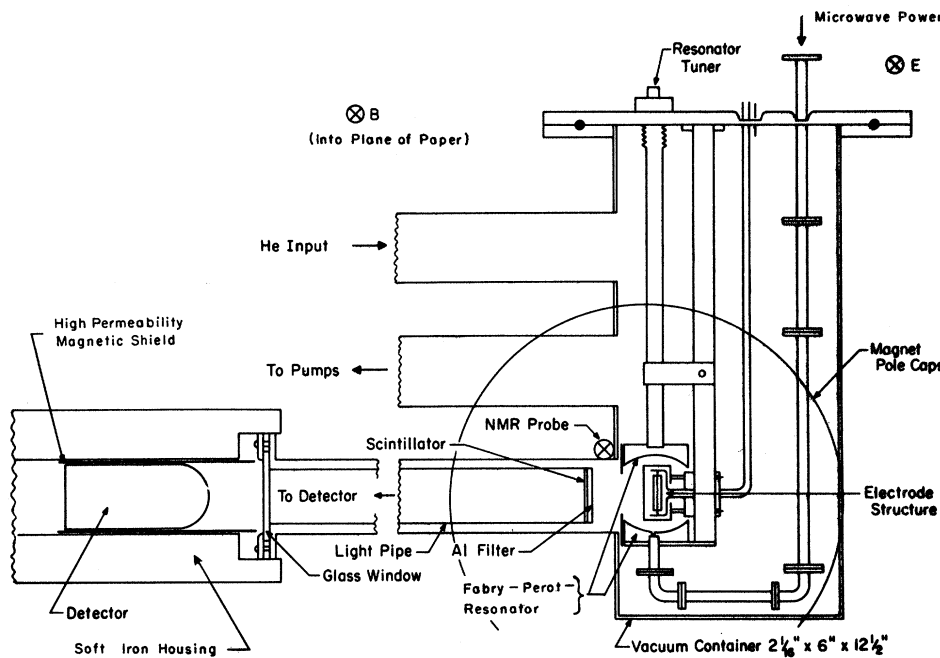

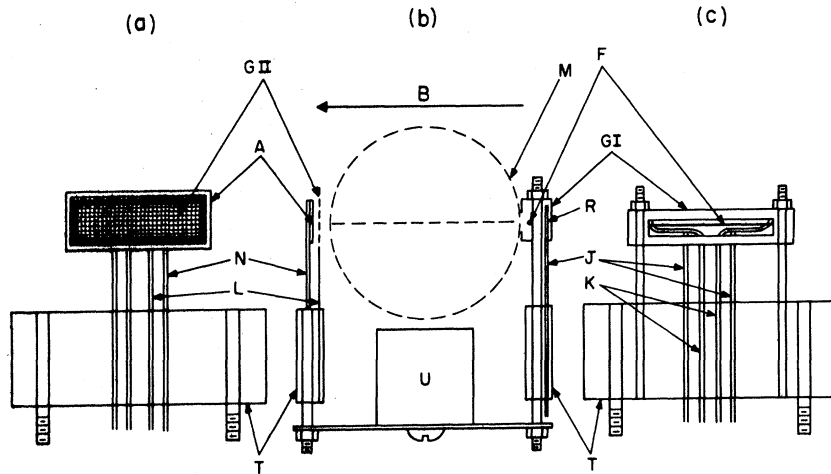FIG. 6. Schematic arrangement of main experimental setup.

(a)   (b)   (c)

FIG. 7. Electrode structure:
(a) inside view—anode structure, (b)
top view, (c) inside view—filament
structure. T is the support glass
blocks, GI electron acceleration grid,
F filament, J electron reflector sup-
ports, K filament supports, R elec-
tron reflector, GII anode screen
grid, A anode, L screen grid sup-
ports, N anode supports, M FPS
plates, and U brass support rod for
the electrode structure.

through the directional coupler D_2 and measured
at the thermistor mount T by the power meter P.
A shift in the rf power meter reading can indicate
(i) a change in klystron output power, (ii) a slight
detuning of the resonator, and/or (iii) a shift in the
zero of the power meter. After leaving the klystron
turned on for a day, the output-power stability of
the klystron was measured to be better than 0.1%
over $\frac{1}{2}$ h. The resonator takes about 2 h after the
filament is turned on to attain thermal equilibrium.
Thereafter, the rf power meter reading was stable
to better than 0.25%, and resonator detuning prob-
lems were rare. The power meter needed to be
reset several times during a run.

D. Magnetic Field

The magnetic field is provided by a magnet (15-
in. pole roots) with caps tapered to 28-cm diam.
The gap length is approximately 65 mm. The mag-
net power supply provides a maximum nominal
output of 13 kW (75 A maximum, 175-V dc). Power-
supply current is stabilized by three feedback loops,
working in three frequency domains, to 1 kHz. The
field coils are aluminum-foil type and are edge
cooled by water circulation.

The magnetic field is measured by a proton reso-
nance absorption apparatus[10] designed to operate
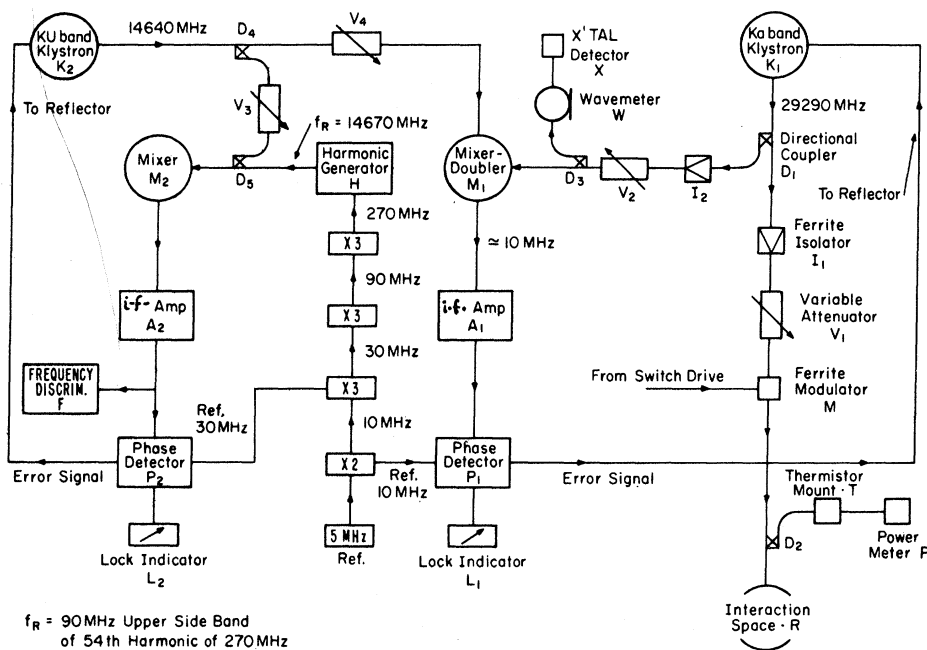at high frequencies. The rf oscillator covers the

FIG. 8. Block diagram
of the rf apparatus.

f_R = 90 MHz Upper Side Band
of 54 th Harmonic of 270 MHz

range of frequencies from 60 to 75 MHz. The sample coil is coupled by a single cable designed to operate at 66 MHz, and is found to be adequate to cover our working region which extends from 63 to 70.5 MHz. The sample (water doped with 0.1% by molar weight manganese chloride) is contained in a small spherical glass bulb (0.32-cm diam). The rf output signal from the oscillator is amplified and fed to a frequency counter. The magnetic field H is measured in terms of the proton resonance frequency ν_p. The width of the proton resonance signal is normally about 200 mG. All possible precautions were taken to reduce the jitter in the oscillator. The oscillator frequency drifts by about 200–300 Hz over a period of $\frac{1}{2}$ h, but this causes no problem since each time a field measurement is made, the oscillator is readjusted. The thermal drift of the magnetic field is insignificant in most of the working fields; it is about a few hundred proton Hz at the high working field.

In the range of working fields the field inhomogeneity is measured to be less than 15 ppm over the dimensions of the quenching region [1 in. along magnetic field (z) axis, 1 in. along resonator (y) axis, and 0.125 in. in observation (x) direction]. The magnetic field was mapped several times at selected values to ensure the stability of the field homogeneity. The field difference between the position of the probe and the center of the quenching region was measured several times during data collection and the field at the probe is lower by 2500 ± 100 proton Hz. Effects of the presence of the system (made of brass) close to the magnet on the field homogeneity were investigated and found to be insignificant.

E. Detection System

The signal to be detected is the flux of 304-Å photons (40.8-eV energy) emitted by the α-state metastable ions that are transferred to the e state due to the inducement of these transitions by the rf power and during their decay to the $1\,^2S_{1/2}$ state (α' or β' corresponding to $m_j = \pm\frac{1}{2}$, respectively) of the ion. The background consists of ionic deexcitation radiation (304-Å and shorter-wavelength photons), atomic deexcitation radiation (500 Å and longer wavelengths), and some visible light of long wavelengths from the heated filament. The detection system is made of three parts:

a. *Aluminum filter*. The purpose of the Al filter is to reduce the visible light and to discriminate the signal light from the large background ultraviolet light by its differential transmittivity to these wavelengths. It is estimated that for the 1700-Å-thick filter used in the experiment, there is approximately 1% transmission of the signal radiation with a low measured transmission ($\simeq 0.001\%$) of the visible light.

b. *Scintillator*. Sodium salicylate, in the form of a coating (surface density $\simeq 0.4$ mg/cm^2), on a glass disk of 25.4-mm diam and located about 10 cm from the interaction space, is the scintillator used in the experiment. The transmitted radiation from the filter is allowed to fall upon this scintillator and is converted into visible light. The fluorescent quantum yield of sodium salicylate is high[11,12] for incident radiation in the range of wavelengths 304–3000 Å ($\simeq 50\%$ for 304 Å).[13] Fluorescence occurs in a wavelength region centered at about 4000 Å.[12] The visible light thus produced is collected by a glass light pipe and guided to the photodetector.

c. *Detector*. The detector phototube has a semitransparent bialkali-coated photocathode, having a spectral sensitivity that matches the fluorescent radiation from the scintillator and S-11 spectral response (manufacturer's specification). It is located in a soft-iron housing as shown in Fig. 6 about 90 cm from the interaction region, and is wrapped with several turns of high-permeability magnetic-shield foil. When operated at 1700 V, the photodetector has an over-all quoted gain of 10^6 and an anode dark current less than 1 nA. The output of this detector is fed to the phase-sensitive detector amplifier and the VTVM.

F. Helium Supply

Commercial helium is purified by passing through cold and charcoal traps, cooled by liquid nitrogen, and is then admitted into the system. The pressure at the input position to the system is monitored by a capacitance manometer. The absolute helium pressure at the interaction space is estimated by interpolation. The pressure can be measured to better than 0.1 mTorr at the normal operating value of 4.6 mTorr. Since the system was of continuous-flow type, the initial drop in the pressure was large ($\simeq 0.5$ mTorr) during the first 1- to 2-h period. Thereafter, the pressure drops slowly, about 0.1 mTorr over a period of 4 to 5 h. Other interpolated pressure values employed in the experiment are around 2.3 and 8.3 mTorr. The capacitance manometer is calibrated for absolute pressure indication by comparison against an oil manometer. If the oil-manometer reading was off by 10%, it would reflect in a corresponding fractional error in the absolute pressure. Such an error would have no influence on the final zero-pressure extrapolated result for the Lamb shift, but it would influence the size of the estimated pressure-dependent corrections (Sec. VII B c).

IV. OPERATING CHARACTERISTICS OF APPARATUS

A. Excitation Curves

The excitation characteristics for the rf induced signals are shown in Fig. 9, for the operating pres-
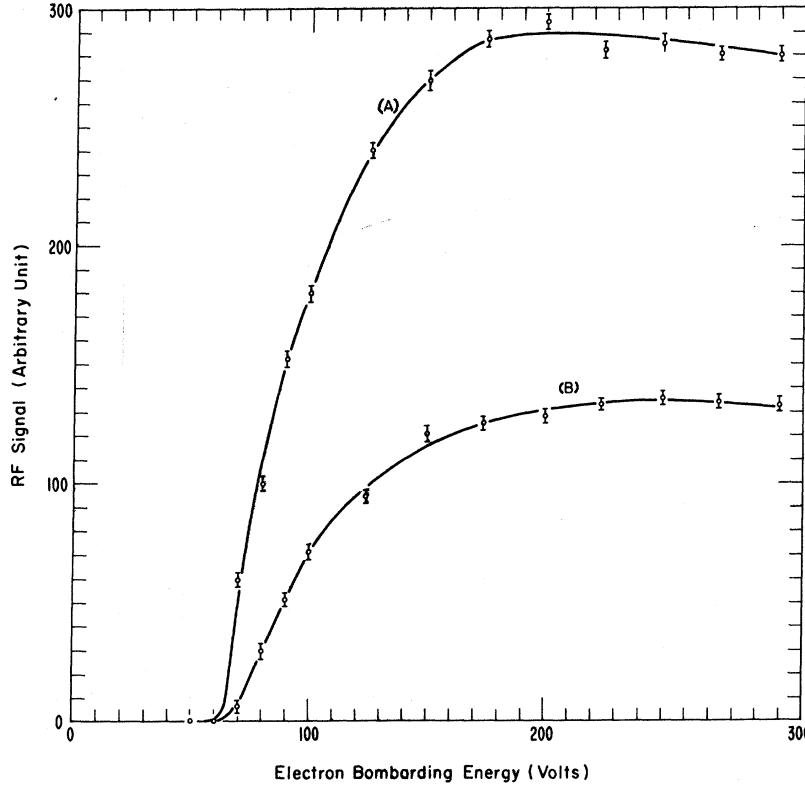
FIG. 9. Excitation curves for the rf induced signal: (A) 4.6 mTorr, (B) 2.3 mTorr, for the He pressure.

sure values 4.6 mTorr (A) and 2.3 mTorr (B), with 4.4 mA for the bombarding-beam current at a magnetic field value close to the resonance center. The sharp increase in signal at 65 V is due to the onset of excitation of the α-state metastable ions. To optimize the rf induced signal, 200 V were chosen for the electron acceleration potential in all experimental runs.

B. Quenching Curves

The rate of decay of the α-state ions to the e state Γ_α due to the presence of rf power can be calculated from the time-dependent perturbation theory,[9] which gives

$$\Gamma_\alpha = \frac{S_0}{h}\frac{e^2}{\hbar c}\,\Gamma_e\frac{|\langle\alpha|z|e\rangle|^2}{(\nu-\nu_0)^2+\mu^2}\;,\tag{1}$$

where S_0 is the incident rf power in erg per cm^2 per sec, Γ_e is the natural decay rate of the P-state ions which is 10^{10}/sec, $\mu=\Gamma_e/4\pi=800$ MHz, $\langle\alpha|z|e\rangle=\frac{1}{2}\sqrt{3}\,a_0$ is the matrix element for the transition $\alpha\to e$, a_0 is the Bohr radius, $\nu=\nu_{\alpha e}$ is the αe transition frequency, and ν_0 is the applied rf frequency. Assuming that all the metastable ions are exposed to the rf power for the same time τ_α, the rf signal strength at a power level P (where the incident energy is S_0 erg/cm^2 sec) is

$$I=I_0(1-e^{-\Gamma_\alpha\tau_\alpha})\;.\tag{2}$$

I_0 is the maximum signal strength at the photodetector for sufficient rf power to yield 100% quenching. Equation (2) may be rewritten in terms of a characteristic power level P_0 as

$$Q=(I/I_0)\,100=(1-e^{-P/P_0})100,\tag{3}$$

where P_0 is defined such that for $P=P_0$, $\Gamma_\alpha\tau_\alpha=1$, and $Q=63\%$. Figure 10 shows a graph of Eq. (3), and experimental results of signal vs power at the resonance line center under the normal operating conditions of 4.4-mA bombarding current and 4.6-mTorr helium pressure. Normalized signal I_0 and power P_0 were adjusted to obtain a best fit to the graph. At the characteristic power level P_0, the linewidth is $\mu(P_0)=1.24\mu\simeq1000$ MHz. In an attempt to reduce the uncertainty $\Delta\nu_0$ with which the resonance center ν_0 can be determined, we chose to operate at the 63% quenching level. The characteristic power levels at the various operating values of helium pressures are determined from the experimental quenching curves. The values of input power to resonator (for 63% Q) thus obtained are 0.38, 0.75, and 2.25 mW at 2.3, 4.6, and 9 mTorr, respectively. Proportionately more power is required at 9 mTorr because of the decrease in τ_α at higher pressure.

At the normal operating conditions (4.6 mTorr for helium pressure, 4.4 mA for bombarding current, and 63% quenching rf power level) the number
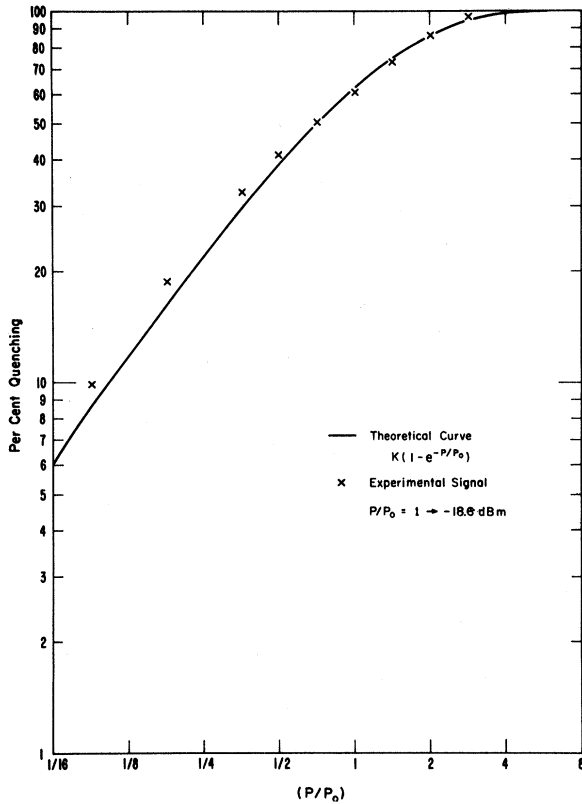
FIG. 10. rf quenching curve for the metastable ions at 4.6 mTorr for the He pressure. The experimental quenching values were adjusted to fit the theoretical curve (dBm = dB above 1 mW).

of events observed at the photocathode is estimated to be slightly over 10^6 per sec. The power available was not sufficient to saturate the transition at the time of precision resonance data; although the klystron was originally able to deliver more power.

V. LINE SHAPE

The time for which an ion is exposed to the rf field is not the same for all ions as assumed in Sec. IV B but it depends upon the position of the ion formation and on the potential distribution along the beam. Equation (2) should be written as

$$I = I_0 \left(1 - \exp \int_0^L \frac{\Gamma_\alpha \, dz}{v(z)} \right) , \qquad (4)$$

where z is the path length of the beam, L is the length of the interaction space (see Fig. 11), and $v(z)$ is the average velocity of all ions at z, produced at positions z', such that $0 < z' < z$; $z = 0$ refers to the position of the anode grid GI. If we approximate the spatial variation of the transition rate Γ_α which has the Gaussian cross section of

the rf field along the z axis by a rectangular function having the same peak value and the same area as the true function, the limits of the integration in Eq. (4) would be from $-\frac{1}{2}d_{eff}$ to $+\frac{1}{2}d_{eff}$, where $d_{eff} = 1.59$ cm is the width of the rectangular function as shown in Fig. 11. Thus detailed knowledge of the potential variation along the beam and the ion velocity as a function of the position is required to calculate the fractional quenching. Since the ion-dynamics problems in these experiments are complicated, we make the simple constant-velocity approximation, under which $\tau_\alpha = d_{eff}/v$ and Eq. (4) reduces to Eq. (2).

There are several processes that govern the motion of the ions in the interaction space, and hence influence τ_α. We will assume that the various ion-removal processes are independent of each other and compute the characteristic removal times for each of them. The magnetic field dependence of these processes and their influence on S will be considered in Sec. VII.

A. Ion-Removal Processes

a. Natural decay. Transitions from the $2\,^2S_{1/2}$ state to the ionic ground state are forbidden ($\Delta l \neq 1$) and the spontaneous decay rate to the $2\,^2P_{1/2}$ state is slow ($\simeq 10^{-6}/\text{sec}$) owing to the small energy separation S. The most probable decay mechanism for the $2\,^2S_{1/2}$ metastable state is the double-photon-emission process for which the lifetime $\tau_\alpha(N)$ = 1.9 msec.[8]

b. Ion thermal and recoil motions. In order to give 4.4 mA of bombarding-beam current, the filament takes a dc heating current of about 6.3 A. The heat radiated by the filament raises the temperature of the interaction space. We have not measured this temperature but assume it to be 400 °K (same as in Ref. 6, where the filament di-
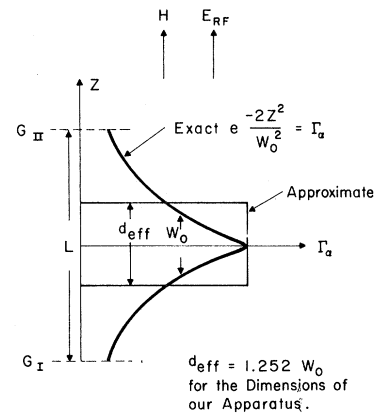

FIG. 11. Spatial variation of the rf transition rate.

mensions and filament current are close to ours while other conditions differ). The z component of the velocity of spiral motion of the ion about the magnetic field lines which is parallel to the magnetic field is

$$v_t = (kT/M)^{1/2} = 0.92 \times 10^5 \text{ cm/sec,} \tag{5}$$

where k, T, and M are the Boltzmann constant, absolute helium temperature, and mass of the helium ion, respectively.

If the recoil velocities of the helium ion are calculated on the basis of the kinematics of electron-atom collisions, they have a large range of values. For incident electrons of 200 eV, the maximum and minimum recoil velocities are[14]

$$V_{recoil}(\text{max}) = 2.52 \times 10^5 \text{ cm/sec ,}$$
$$V_{recoil}(\text{min}) = 0.21 \times 10^5 \text{ cm/sec .} \tag{6}$$

Since one does not know the distribution of recoil velocities, an average velocity cannot be assigned with the above knowledge. So we set the recoil momentum of the ion equal to the average momentum of the ejected electron, which is $z_{eff}\alpha mc$,[15] where $z_{eff} = 1.69$, the effective nuclear charge, α is the fine-structure constant, m is the electronic mass, and c is the speed of light. For the average ion recoil velocity this gives

$$\bar{v}_r = z_{eff}\,\alpha(m/M)c = 0.506 \times 10^5 \text{ cm/sec .} \tag{7}$$

The resultant velocity with which ions are drained out of the interaction space is then obtained from the sum of kinetic energies corresponding to thermal and recoil motions and is

$$v_L = (\tfrac{1}{3}v_t^2 + v_r^2)^{1/2} = 0.963 \times 10^5 \text{ cm/sec .} \tag{8}$$

The dominating contribution to v_L comes from the thermal effect. The speed of the spiral motion of the ions around the field lines due to thermal and recoil motions is

$$v_T = \sqrt{2}\,v_L = 1.375 \times 10^5 \text{ cm/sec .} \tag{9}$$

The ion-removal time due to thermal and recoil motions is

$$\tau_\alpha(TR) = d_{eff}/v_L = 16.5 \ \mu\text{sec .} \tag{10}$$

c. Space-charge effects. Prior to the admission of the helium gas into the system, the presence of the electron beam produces a potential well whose depth depends upon the beam current. At 4.4-mA beam current this is estimated to be approximately 20 V by considering the electronic-charge sheet and the nearest parallel grounded metal surface as a parallel-plate capacitor. When helium gas is admitted into the system, ions are produced uniformly along the length of the beam. Since the average translational and recoil motional energy of the beam is small ($\simeq 0.02$ eV), all ions produced

between GI and GII are initially trapped, neutralizing the potential depression. Thereafter, a positive ionic space charge builds up until ions are removed towards the filament at the same rate as they are produced. The mean velocity of the secondary electrons liberated in the gas is high ($z_{eff}\alpha c = 2.7 \times 10^8$ cm/sec) and so they leave toward the anode quickly, making negligible contribution to the resultant charge density of ions and primary electrons. To obtain approximate solutions to the charge densities and space-charge fields within the interaction space, we used Helm, Spangenberg, and Field's formalism.[16] At the normal operating conditions of the apparatus we estimate $\sigma_{e1} \simeq 1.03 \times 10^9$ electrons/cm^3, $\sigma^+(0) \simeq 3.83 \times 10^9$ ions/cm^3, $R \simeq 4.2 \times 10^{15}$ ions/sec cm^3, where σ_{e1} is the primary beam electron density, $\sigma^+(0)$ is the ion density close to anode position, and R is the ion-production rate. The transverse space-charge field E_{sx} is zero in the plane of symmetry and is maximum ($\simeq 63$ V/cm) at the edge of the ion cloud. The longitudinal space-charge field E_{sl} has longitudinal variation similar to $\sigma^+(z)$ which is gradual up to a position close to the filament (see Ref. 16) where it varies quite rapidly to join the GI potential smoothly. Upon the assumption that this field varies at a uniform rate over the length L, it is estimated to be about 25 V/cm.

However, the mean lifetime for the ion removal is estimated by the principle of charge conservation, according to which

$$LR = \sigma^+(m)\bar{v} , \tag{11}$$

where $\sigma^+(m)\,[\simeq 0.85\sigma^+(0)]$ is the mean ion charge density, $\bar{v}$ is the average longitudinal velocity of the ions (5.75×10^6 cm/sec), R is the ion-production rate, and L is the separation between GI and GII (4.45 cm).

At the normal operating conditions of the apparatus we have

$$\tau_\alpha(SP) = d_{eff}/\bar{v} = 0.276 \ \mu\text{sec.} \tag{12}$$

The transverse space-charge electric field (along the x axis or the observation direction) is zero along the beam axis and increases linearly to its maximum value at the edge of the charge cloud so ions move in crossed electric and magnetic fields and exhibit cycloidal motion. The transverse space-charge electric field is always normal to and away at the edges of the charge cloud in such a way that the ions are not lost to the ion beam in the y direction (resonator-axis direction).

d. Stark quenching. The external electric fields mix the α state with the adjacent short-lived P states and thus reduce the lifetime of the α state. The decay constant of the mixed state can be calculated through time-dependent perturbation theory [HI, Eq. (16)] and is given by

$$\Gamma_\alpha = \sum_i \frac{\Gamma_P |\langle \alpha | \vec{E} \cdot \vec{r} | i \rangle|^2}{\hbar^2 (\omega_{\alpha i}^2 + \frac{1}{4}\Gamma_P^2)} \, , \tag{13}$$

where E is the mixing electric field, $\omega_{\alpha i}$ is the angular separation between the states α and i, and Γ_P is the P-state decay rate. The mixing electric fields arise from the space-charge effects $(E_{1s} = \frac{1}{2}E_{smax} = 31.4\text{V/cm})$ and motional effects $(E_m = |\vec{V}_\perp \times \vec{H}/c| = 21.6\text{ V/cm})$. The perpendicular component of velocity required to calculate the motional electric field is due to the thermal and recoil effects and a magnetic field value corresponding to the resonance center has been used in the computation. The net transverse electric field has been computed with due attention to the fact that E_m is rotating in the xy plane while E_{1s} is along the x direction. The transverse electric field $(\simeq 42.4\text{ V/cm})$ and the longitudinal space-change electric field $(\simeq 25\text{ V/cm})$ can couple the state α with the neighboring states f, c, a, e, and b where a, b, c, d are the magnetic substates of the $2\,^2P_{3/2}$ state. The e and f states are close in energy to α, the dominant coupling being between α and f, for which $\Delta m = 1$. At the normal operating conditions the lifetime of the α states, from these considerations and allowing for the fact that the transverse electric fields should have been added like vectors, is

$$\tau_\alpha(S) = 1.64 \ \mu\text{sec.} \tag{14}$$

Note that the longitudinal space charge is actually much less than was assumed over a major portion of the interaction-space length.

e. Collision quenching. Metastable ions can be lost through encounters with normal helium atoms. Since the background pressure is quite low $(4 \times 10^{-4}\text{ mTorr})$ and the operating range of helium pressure is from 2.3 to 8.5 mTorr, we only need to consider collisions with helium atoms.

Metastables can be lost in an elastic collision with neutral atoms by the following: (i) The metastable ion returns to the ionic ground state and the excitation energy is transferred to the atomic electron resulting in its ejection and (ii) the passage of an ion near a neutral atom produces a dipole field which will have a spectral intensity at each of the frequencies $\mathbb{S}$ and $\Delta E - \mathbb{S}$ so that transitions are indeed to the short-lived P states. Lipworth and Novick[7] report estimates of cross section for the above processes to be $15.9\pi a_0^2$ and $34.4\pi a_0^2$, respectively, resulting in a total cross section of $50.3\pi a_0^2$. At our normal operating pressure of 4.6 mTorr the corresponding mean free path is 1.41 cm, resulting in an ion-removal time of

$$\tau_\alpha(IA) = 0.245 \ \mu\text{sec.} \tag{15}$$

Assuming the various processes to be independent, the time of exposure of a metastable ion to

the rf field may be written as

$$\frac{1}{\tau_\alpha} = \frac{1}{\tau_\alpha(N)} + \frac{1}{\tau_\alpha(TR)} + \frac{1}{\tau_\alpha(ST)} + \frac{1}{\tau_\alpha(IA)} + \frac{1}{\tau_\alpha(0)} \, , \tag{16}$$

where $\tau_\alpha(0)$ represents other processes of negligible importance. Clearly the longitudinal space-change electric field plays a dominant role in the ion-removal mechanism. Their sum gives

$$\tau_\alpha = 0.126 \pm 0.010 \ \mu\text{sec.} \tag{17}$$

A 10% error has been assigned in view of the several assumptions in estimates.

The value for the ion-removal time has been computed in Appendix A, using $\tau_\alpha \Gamma_\alpha = 1$ for the 63% quenching power level, from which

$$\tau_\alpha = 0.11 \pm 0.02 \ \mu\text{sec.} \tag{18}$$

Such an agreement between observed and calculated values for τ_α may be fortuitous but supports the predominance of space-charge effects in the ion-removal processes.

B. Panoramic Resonance Curves

For sufficiently low-quenching rf power levels $(\Gamma_\alpha \tau_\alpha \ll 1)$ Eq. (2) reduces to

$$I = I_0 \Gamma_\alpha \tau_\alpha = K/[(\nu - \nu_0)^2 + \mu^2] \, , \tag{19}$$

where

$$K = (S_0/h)(e^2/\hbar c)\Gamma_e |\langle \alpha | Z | e \rangle|^2 I_0 \tau_\alpha \, . \tag{20}$$

Since the experiment is done in a magnetic field and the magnetic mixing of e and b states results in the magnetic field dependence of $|\langle \alpha | Z | e \rangle|^2$, we need to insert a correction factor $C_{\alpha e}$ for the αe-matrix-element variation in expression (19). The signal is the flux of 304-Å radiation emitted (in x direction) by the decay of the e state to the ionic ground state. The matrix elements in this decay require another correction factor (details concerning these correction factors are in Appendix B). The Zeeman transition frequency $\nu_{\alpha e}$ in expression (19) is given by[9]

$$\nu_{\alpha e} = \mathbb{S} + \tfrac{1}{2}(g_s - g_l)(\mu_B H/h) + \tfrac{1}{2}(\Delta E/h)$$
$$\times [(1 + \tfrac{2}{3}\chi + \chi^2)^{1/2} - 1] \, , \tag{21}$$

where

$$\chi = (g_s - g_l)\mu_B H/\Delta E \ (2\,^2P_{3/2} - 2\,^2P_{1/2}) \, , \tag{22}$$

g_s is the electron-spin g value including the anomalous part, g_l is the orbital g value corrected for nuclear motion, and μ_B is the Bohr magneton. ΔE is the fine-structure separation in energy between the $2\,^2P_{3/2}$ and $2\,^2P_{1/2}$ levels. Equation (21) may be rearranged without affecting the line shape as

$$\nu(H) = (\nu_{\alpha e} - \mathbb{S}) = \tfrac{1}{2}(g_s - g_l)(\mu_B H/h)$$
$$+ \tfrac{1}{2}(\Delta E/h)[(1 + \tfrac{2}{3}\chi + \chi^2)^{1/2} - 1] = \nu(\nu_p) \tag{23}$$

and $\mu_B H$ can be rewritten as

$$\mu_B H = 2\pi(\mu_B/\mu_e)(\mu_e H/\gamma_p H)\nu_p ,\qquad(24)$$

where μ_e/μ_B is the electron magnetic moment in Bohr magnetons[17] and $2\pi(\mu_e H/h\gamma_p H) = \omega_e/\omega_p$ is the ratio of the cyclotron frequency of a free electron to the proton resonance frequency measured in the same magnetic field H.[18] Once the resonance line center $\nu_0'(\nu_p)$ is located in the magnetic space, it is set equal to ν_{rf} and $\mathcal{S}$ is calculated through

$$\nu_0'(\nu_p) = \nu_{rf} - \mathcal{S} .\qquad(25)$$

Thus the theoretical line shape at low-rf power level, containing the correction for the matrix-element variation $C_{\alpha e}$, the signal-light intensity redistribution C_{eg}, and the Zeeman curvature in an exact fashion is

$$I(\nu_p) = K C_{\alpha e}(\nu_p) C_{eg}(\nu_p)/\{[\nu(\nu_p) - \nu_0']^2 + \mu^2\}$$

$$= I_0 \Gamma_\alpha' C_{eg}(\nu_p)\tau_\alpha ,\qquad(26)$$

where

$$\Gamma_\alpha' = \Gamma_\alpha C_{\alpha e}(\nu_p) ,$$

$$\nu_0' = \nu_{rf} - \mathcal{S} .\qquad(27)$$

At all different operating conditions of the experiment the observed signal levels at the selected magnetic field values are fitted to the line-shape expression (26) by a least-squares method. The required corrections for deviations from the low-power quenching approximation were made later. A typical Lamb-shift resonance line at the normal operating conditions of the apparatus is shown in Fig. 12. The width of the line is in close agreement with calculation and is close to 1000 MHz for 63% quenching.

A true description of the line shape at any quenching power level is given by

$$I = I_0[1 - e^{-\Gamma_\alpha C_{\alpha e}(\nu_p)\tau_\alpha}] C_{eg}(\nu_p) .\qquad(28)$$

A normalization scheme that employs power levels appropriate to 35 and 95% quenching was used to check the precision measurements with ν_{rf} = 29 290.00 MHz. Here the signal ratios $I(35\% \, Q)/I(95\% \, Q)$ are least-squares fitted to the ratio curve

$$Z(\nu_p) = \frac{I(35\% \, Q)}{I(95\% \, Q)} = C\frac{[\nu(\nu_p) - \nu_0']^2 + \mu_{hQ}^2}{[\nu(\nu_p) - \nu_0']^2 + \mu_{lQ}^2} ,\qquad(29)$$

where C is an arbitrary constant, and μ_{lQ} and μ_{hQ} are linewidths corresponding to 35% Q and 95% Q power levels, respectively.

VI. PRECISION RESONANCE DATA PROCEDURE

A single experimental run consists of signal measurements at eight selected magnetic field values (four pairs), nearly symmetrical on either side of the βf crossing field. These field values

range from 63.30 to 70.15 proton MHz (which correspond to about 14.87–16.48 kG), where the field homogeneity (15 ± 5 ppm over the quenching region) is the same. The pair of field values closest to the resonance center mainly serve to establish the resonance peak, while the remaining three pairs, selected in the regions of high slope of the resonance line, determine the line shape and hence the center. The course of travel among the four pairs of fields is zigzag, being different runs, so that the influence of any time-dependent drifts on the line center is reduced. The scheme of travel is also such that the initial pair is repeated at the end, and hence provides a check on the stability of the system during the run.

After turning on the system, 2–3 h were allowed for the parameters not servocontrolled to stabilize. "Turning on the system" refers only to the bombarding-beam current, helium pressure, photodetector power supply, and the rf power modulator since the rest of the system was run continuously in the absence of repair problems. With the best Al filter in the system, the time allotted for each signal recording is 9 min for the 8.5- and 4.6-mTorr runs and 15 min for the 2.3-mTorr runs. About 6–10 min were allowed between two signal records in order to reset and allow the magnetic field to stabilize, check the rf power-level resonator stability and electron-beam current, and record any observed fluctuations. So the total time required to collect the data alone ranges from 4 to 6 h for a single run. The operating pressure values for the runs are measured at the end of the run. There are slight variations in pressure between
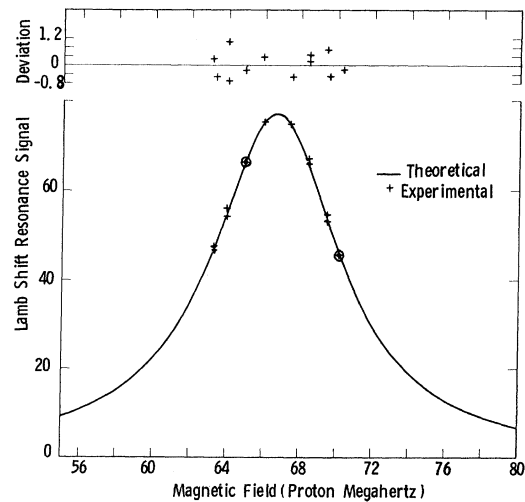

FIG. 12. Panoramic resonance curve for the αe-transition resonance signal as a function of the magnetic field. At the top the deviation of experimental results from calculated values are shown on an expanded scale.

various runs in the same pressure group, but this causes no problem since measured pressure values were used in extrapolating to zero pressure for the Lamb shift. In the normalization measurements, a run has a similar procedure, except that the signals at a particular magnetic field value are recorded first with low quenching power followed by the high quenching power. A time constant of 30 sec was used in all runs for the phase-sensitive detector-amplifier.

Before processing the data, corrections for the photomultiplier gain variation with magnetic field and other observed parameter fluctuations are applied. The data are then least-squares fitted to the theoretical line-shape expression (26). The fit gives the line center in terms of

$$\nu_0'(\nu_b) = \nu_{\alpha e} - S \text{ at } \nu_{\alpha e} = \nu_{rf} = 29\,290.000 \text{ MHz} ,$$

and the linewidth μ.

VII. CORRECTIONS AND UNCERTAINTIES

Any effect that has an influence on the observed line shape would also influence the final result for the resonance line center. In a precision experiment such as this, any and all such possible effects must be carefully considered and appropriate corrections must be made to the Lamb shift. We consider them in four groups; the first one includes all effects that are intrinsic to a single metastable ion placed in an external magnetic and electric field, the second group is concerned with effects that depend upon an assemblage of atoms and ions, the third group includes all effects due to deviations from having an ideal apparatus in the experiment, and the fourth group considers corrections associated with the method of analysis. It should be noted that since the experimental values grouped at three different pressure values are least-squares fitted to a straight line, pressure-dependent corrections are partly removed. Our consistent choice of 63% quenching at the three pressure values might not have permitted a complete elimination of these corrections.

A. Effects Intrinsic to the Ion

a. Shifts in α, e state energy. The presence of external magnetic and electric fields in the interaction space give rise to shifts in the energy levels of the fine structure, including α and e states. The magnetic shift is the Zeeman effect of the fine structure. The Zeeman transition frequency $\nu_{\alpha e}$ loses its linearity at sufficiently strong magnetic fields [note that the presence of the square-root term in expression (21) gives rise to the Zeeman curvature]. Since our line expression [(26)] contains $\nu(\nu_b)$ in an exact fashion we need not apply a separate correction. If a linear approximation had been made to this frequency a correction of − 0.94

MHz would have been required for S.

Electric fields give rise to Stark shifts in the energy levels of the fine structure, including α and e states. The Stark shift in the energy level i due to a field of E V/cm is

$$\Delta W_i = \sum_n \frac{|\langle n|e\vec{E} \cdot \vec{r}|i\rangle|^2}{E_n - E_i} . \tag{30}$$

All necessary matrix elements that couple α and e to the neighboring states are evaluated by Lamb (HIII, Table IV) for hydrogen and these can be used for He$^+$ after modification for Z. The electric fields seen by a single ion at a temperature $T\,°K$ in the presence of an external magnetic field and an electron beam current of 4.4 mA are of importance here and both are transverse to the magnetic field. At the resonance line center, the transverse-motional electric field E_m due to thermal and recoil effects is estimated to be 21.6 V/cm. This is a rotating vector in the xy plane but remains perpendicular to the H direction. The transverse space-charge electric field E_{sx} computed from the net positive charge density is maximum at the edge of the beam and zero at the symmetry plane changing linearly with distance in between. E_{sx}(max) is estimated to be 63.0 V/cm at 4.4 mA. The resultant x and y components of the transverse E field are taken to be

$$\left|\vec{E}_m + \tfrac{1}{2}\vec{E}_{sx}(\max)\right| \pm \tfrac{1}{2}\left|\vec{E}_{sx}(\max)\right| \text{ and } \left|\vec{E}_m\right| .$$

Note that while E_{sx} is constant, E_m is rotating. These transverse electric fields can couple α with f and β with e, elevating both α and e in energy, but e more than α. Since the actual direction and magnitude of the resultant electric field on the ion depends on directions and magnitudes of E_m and E_{sx}(max), we have taken 8.8±45.6 V/cm for the resultant magnitude to include all possibilities and allow for uncertainties in the recoil velocities. The resultant correction is + 0.004 ± 0.118 MHz in S.

b. Change in α, e matrix element. The theoretical line-shape expression (26) contains the exact formula for $C_{\alpha e}$, the variation of $|\langle \alpha|Z|e\rangle|^2$ with the magnetic field. The range of magnetic fields used in this experiment is large ($\simeq 1.6$ kG) and the matrix-element variation produces a significant distortion in the line. If a separate correction had been made for this effect it would amount to about − 8.06 MHz in S.

Similarly, the transverse electric fields mixing α with a and c would require corrections due to the field dependence of $C_{\alpha a}$ and $C_{\alpha c}$. These would actually enter in overlap corrections to be discussed.

c. Changes in final-state density. The transition probability per unit time for the state e to the ionic ground state by electric dipole transitions

is of order 10^{10} sec^{-1} and is proportional to the third power of the frequency for this transition. In an external magnetic field the matrix elements for this transition as well as the energy levels of the initial and final states depend on the magnetic field. The former effect is considered in Sec. VIIB e while the latter, which is related to the density of e states, is of concern here. The fractional change in the frequency over the range of working magnetic fields is about one part in 10^8, and the resulting fractional change in transition probability is three parts in 10^8. Hence, the corresponding fractional change in the density of the final state e is negligible.

d. Overlap correction. The applied rf field, in addition to inducing the αe transition, may stimulate the transitions βf, βe, and αf, and produce distortion in the desired αe resonance which can be excited at higher intensities of the rf field. βf has the same polarization as αe. However, the rf was chosen so that the center of the αe resonance line lies close to the βf crossing field. Thus the overlap effect of the βf transition upon αe is symmetrical about the applied rf value, and is small because of the large separation between the αe resonance center (29 290.00 MHz) and the βf resonance center (0.00 MHz). To excite the transitions αf and βe, an electric field vector with σ polarization is needed. Slight misalignment in the apparatus design or canted magnetic field can give rise to such a component.

The magnetic field was swept at the applied rf frequency through the αf transition and the relative intensity of αf compared to αe was measured, from which we infer a 6% σ component in the applied rf power. The maximum available magnetic field is not sufficient to be able to sweep through the βe line. The αf and βe resonance centers are on the lower and higher sides of the αe resonance center, respectively; however, overlap from the αf transition is weaker at higher quenching levels since a smaller number of α-state ions are available to contribute, while the same is not true with β ions. Corrections and uncertainties are taken to be

$$\theta \delta \omega(\alpha f) + \delta \omega(\beta e) \pm \tfrac{1}{2} \delta \omega(\beta e) ,$$

where $\theta = 1$, $\tfrac{1}{2}$, and 0 for the three quenching power levels.

With 35, 63, and 95% for the power levels used under normal conditions of helium pressure and bombarding beam current, the total corrections are then -0.017 ± 0.058, $+0.096 \pm 0.113$, and $+1.231 \pm 0.616$ MHz, respectively. The fact that there exists a cancellation of effects from αf and βe makes the corrections insensitive, to a large degree, for a small error in the fractional σ-component value. The S states in the higher levels of

the ion are not metastable (life times $\simeq 10^{-8}$ sec) and so these are not overlap contributions due to induced transitions in these states.

e. Signal-intensity redistribution. The correction factor $C_{\theta f}$ in the line-shape expression removes the effect of variation with the magnetic field of the matrix elements involved in the decay of the e state to the ionic ground state (see Appendix B). A separate correction would have amounted to -1.7 MHz in $\mathcal{S}$.

f. rf Stark effect. Lamb developed expressions for calculating the shift in frequency due to the presence of rf fields HIII, p. 274). From this analysis, the desired shift in the angular frequency $\omega(\alpha e)$ is given by

$$\Delta \nu = \Delta \omega / 2\pi = \Gamma_\beta \, \tau_\alpha^{-1}/16\pi\omega(\alpha e) , \qquad (31)$$

where $\omega(\alpha e)/2\pi = 29\,290$ MHz (resonance frequency). Under normal operating conditions the value obtained for $1/\tau_\alpha$ from the calculation in Sec. V A is 7.97×10^6/sec, and from the rf power used it is 9.1×10^6/sec. The mean of these values is 8.54×10^6/sec and an uncertainty of $(1/2\tau_\alpha)$ was used to obtain the required corrections at the three power levels employed. The corrections in $\mathcal{S}$ are then -0.060 ± 0.030, -0.117 ± 0.058, and -0.345 ± 0.172 MHz, respectively.

B. Effects Characteristic of Assemblage of Atoms or Ions

a. Field dependence of available α-state ions. The number of available α-state ions for rf quenching depends upon the number of available helium atoms in the interaction space, electron flux density, and the cross section for production of the α ions by the electron-atom collisions. For constant energy of electrons, the ionization efficiency (hence cross section for production of metastables) is independent of the magnetic field value. This is due to the fact that while the diameter of the helical path of the electrons decreases with increasing magnetic field value, the electron spiraling frequency increases in such a way that the electron path length is independent of the magnetic field. Since the magnetic field does not impart additional energy to the electron, its energy is also independent of magnetic field. This results in a field-independent value of the production rate of the α-state ions. The number of helium atoms available for ionization is also constant as indicated by the pressure monitoring apparatus, once equilibrium conditions are established in the apparatus as far as the pressure and temperature are concerned. By the use of a proper procedure for precision resonance data as described in Sec. VI, effects due to gradual drifts in the pressure and temperature are eliminated.

b. Stark effect due to ionic space-charge fields.
An assemblage of ions gives rise to space-charge
electric fields both of transverse (E_{sx}) and longitu-
dinal (E_{sl}) character. The transverse fields have
a similar effect as described in Sec. VII A a and
the longitudinal fields couple α and e such that
$\delta\omega_{\alpha} = -\delta\omega_{e}$, where the Stark shift $\delta\omega$ is calculated
according to the expression (30). Since the experi-
mental result for the Lamb shift $\mathcal{S}$ is obtained by a
zero-pressure extrapolation, the calculated shifts
do not influence the final result.

At normal operating conditions the magnitude of
the resultant transverse field is 8.8 ± 45.6 V/cm
and the magnitude of the longitudinal field is
12.5 ± 12.5 V/cm. The resultant correction due
to the ionic space charges is then $+0.090 \pm 0.252$
MHz, neglecting the effect of the magnetic field
on the space-charge electric fields.

*c. Field dependence of space-charge motions
and collisions quenching.* We have used the Helm-
Spangenberg-Field formalism[16] and change conser-
vation principle to estimate $\tau_{\alpha}(SP)$ in Sec. V A c.
According to this formalism although the ion beam
is compressed in the transverse direction (due to
reduced ion orbit radius) as a higher magnetic
field, the ion-removal time $\tau_{\alpha}(SP)$ is not affected
since the ion charge density and ion-production rate
have similar dependences on the ion-beam thick-
ness. The longitudinal space-charge electric field
is independent of the beam compression effect and
this results in a magnetic-field-independent colli-
sion quenching cross section.

The possibility of a shift exists in the observed
resonance center due to the perturbation of the
$2S$-$2P$ system of levels during a collision process.
The perturbing electric field is produced by an in-
duced dipole moment in the neighboring neutral
atom. At a helium pressure of 4.6 mTorr, Lip-
worth[19] estimates a shift of 0.25 MHz for such a
process. Since the relative ion velocity in our ap-
paratus is approximately twice as much as Lip-
worth's apparatus due to the higher space-charge
fields, we may have a slightly larger shift due to
this effect. We assign an uncertainty of ± 1.0 MHz
for these effects, although a better analysis could
reduce such a large uncertainty.

*d. Field dependence of resonance radiation
absorption.* The signal light (304-Å radiation) as
it escapes in the direction of the detector can
be resonantly absorbed by the ground-state ions.[4]
If this resonance radiation absorption changes with
magnetic field it would result in a shift in the reso-
nance center. The resonance radiation absorption
is estimated to be an insignificant process at the
existing ion densities in the apparatus and thus is
a negligible influence on the results.

e. Pressure-calibration uncertainty. As de-
scribed in Sec. III F, an error in the absolute pres-
sure calibration by 10% would contribute to an error
in the estimated pressure-dependent corrections.
Such an error would contribute to an uncertainty
in a pressure-gradient comparison as well as to
corrections characteristic of assemblage of ions.
Allowance is made to include this contribution
while assigning the ± 1 MHz uncertainty in Sec.
VII B c.

C. Deviations from Ideal Apparatus

a. Magnetic-field-inhomogeneity correction.
The field difference between the probe position and
the interaction space was measured several times
during the course of precision resonance data.
This required a correction of -0.570 ± 0.025 MHz.

b. rf power variation. Variations in the residual
magnetic field values at the positions of the Ka-
band klystron, ferrite isolators, and ferrite modu-
lator (which are about 6, 20, and 30 G, respective-
ly, at the resonance-center field value) with ex-
ternal field can lead to a magnetic field dependence
of the rf power level in the quenching region. It
was found that the rf power is higher at the lowest
working field rather than at the highest working
field by 5 parts in 10^4. Owing to the low rf power
variation, a correction factor of -0.050 ± 0.050
MHz was assigned $\mathcal{S}$.

*c. Grid transmission (bombarding-beam current)
variation.* The primary electrons have a thermal-
velocity component that is perpendicular to the
direction of the magnetic field. Thus they move
in tight spirals around the flux lines and the spiral
radius becomes smaller and the current density
larger at a higher magnetic field value. This may
result in a larger fraction of the beam current
being intercepted by the acceleration grid wires
at higher fields. The total electron-beam current
reaching the anode and the anode screen grid as a
function of magnetic field, both with and without
helium in the system, were measured. The mea-
surements show the bombarding-beam current
traversing across the interaction space to be
higher at lower magnetic field values. The result-
ing correction due to this effect is -0.250 ± 0.050
MHz.

d. Photomultiplier gain variation. The residual
field at the position of the photocathode changes
from 40 to 65 mG when the external magnetic field
is changed from the lowest (14.98 kG) to the highest
(16.56 kG) working-field value. This results in a
variation of the gain of the photomultiplier with
the magnetic field which was measured several
times. The gain is higher by 0.7% at the lowest
working field than at the highest working field.
The observed signal values at the various working-
field values were corrected for this gain variation
before being processed. The uncertainty associ-
ated with this is estimated from the scatter in the

TABLE I. Precision experimental results. $\Delta\nu_0$ is the weighted mean standard deviation for the group of runs. Group V has a filament that has been displaced by 1 mm at center. Groups V, VI, and VII used a replaced aluminum filter which resulted in a lower signal-to-noise ratio. In group VII power broadening contributes to further reduction of signal-to-noise ratio.

Group No.	Filament No.	No. of runs	He pressure (mTorr)	Operating conditions Beam current (mA)	rf level % Q	$\nu_0 \pm \Delta\nu_0$ (MHz)
I	1	13	2.4	4.4	63	15 244.657 ± 0.395
II	2	7	2.5	4.4	63	15 245.059 ± 0.700
III	1	9	4.7	4.4	63	15 244.243 ± 0.547
IV	1	9	8.3	4.4	63	15 244.125 ± 0.629
V	3	8	4.8	4.4	55 and 82	15 243.423 ± 1.203
VI	4	6	4.6	4.4	35	15 243.230 ± 0.975
VII	4	6	4.6	4.4	95	15 244.652 ± 2.002
VIII	4	6	4.6	4.4	35/95	15 243.821 ± 1.560

gain calibration data as ± 0.160 MHz.

e. Field dependence of quantum convector. The magnetic field dependence of the fluorescent radiation flux from the sodium salicylate quantum converter has been checked to be constant in the operating range of field values to 1 part in 10^3. The necessary correction for this is -0.125 ± 0.125 MHz in S. This correction is made on the basis of results of a separate experiment where a small increase in the fluorescent light with the magnetic field[20] is observed at a lower range of fields.

f. Filament bending effect. The filament carries a dc current of 6.3 A and is located in a strong magnetic field. If the filament distortion depends upon the magnetic field intensity, then the position of the ion beam relative to the rf power distribution changes and can lead to a shift in the resonance center. Great care was exercised when installing the filament symmetrically with respect to the resonator structure. The filament is mounted under tension (once measured $\simeq 4$ lb) so that the bending effect is greatly reduced. Precision resonance data are obtained with four different filaments. One of these filaments (No. 3, see Table I) was deliberately displaced by 2 mm at one end of the filament so that displacement is 1 mm at the center in order to enhance the filament bending effect. The results of this group show no significant difference. In view of the internal agreement of the results, no correction was made.

g. Magnetic field effects on associated electronics. The racks containing most of the electronic equipment are approximately 2 m away from the center of the magnet and each of the instruments, the phase-sensitive detector-amplifier, reference oscillator, VTVM used for background monitoring, and recorder are checked for an over-all field dependence. Since the limit of detectability is taken to be 0.1%, a correction of -0.125 ± 0.125 MHz is applied to S.

D. Corrections Associated with Method of Analysis

a. Least-squares calculation. The experimental signal levels S_i obtained as described in Sec. VI are least-squares fitted to the theoretical line shape of expression (26) by a least-squares technique. Since the results are obtained at three distinct values for the helium pressure an attempt was made to use the line-shape expression

$$I(K, \tau, \nu_0, \mu; \nu_{pi}) = \frac{KC_{ae}(\nu_{pi})(1 + \tau\Delta\nu_{pi})}{[\nu(\nu_{pi}) - \nu_0']^2 + \mu^2}, \quad (32)$$

where

$$\Delta\nu_{pi} = \nu_{pi} - \nu_0'. \quad (33)$$

Least-squares fitting of the experimental data then involves determination of the parameters β_j, where $\beta_1 = K$, $\beta_2 = \tau$, $\beta_3 = \nu_0'(\nu_p)$, and $\beta_4 = \mu$, such that the sum over the number of data points n

$$G = \sum_{i=1}^{n} (S_i - I_i)^2 \quad (34)$$

is a minimum. In addition to the parameters β_j, the calculation gives the variance of each parameter $\sigma^2(\beta_j)$ and of data $\sigma^2 = G(n-4)^{-1}$. The use of expression (32) indicated τ to be a small quantity. Furthermore, the variance in the data obtained with $\tau = 0$ [expression (26)] was less than the variance obtained with expression (32). Hence, a three-parameter fit was used in all experimental runs. The necessary weighting factors w_i are obtained from the standard deviations $\sigma_{\nu_0 i}$ and are the inverse squares of the standard deviations. The results obtained at various pressures are least-squares fitted to a straight line according to

$$Y_i = a + bX_i, \quad (35)$$

where Y_i and X_i represent the resonance center and the operating helium pressure. a and b are determined such that the sum over the total number of runs n

TABLE II. rf power-dependent corrections to the observed resonance centers. $\nu_0'(\nu_p) = \nu_{rf} - S$ (MHz).

	$\eta = 0.5$ (35% Q)	$\eta = 1$ (63% Q)	$\eta = 3$ (95% Q)
Observed resonance-center values (Table I)	$15\,243.230 \pm 0.975$	$15\,244.243 \pm 0.547$	$15\,244.652 \pm 2.002$
Overlap correction (Sec. VII A d)	0.017 ± 0.058	-0.096 ± 0.113	-1.231 ± 0.616
rf Stark effect (Sec. VII A f)	0.060 ± 0.030	0.117 ± 0.058	0.345 ± 0.172
Observed corrected resonance centers	$15\,243.407 \pm 0.977$	$15\,244.164 \pm 0.562$	$15\,243.766 \pm 2.135$

$$H = \sum_{i=1}^{n} w_i (Y_i - \sigma_{\nu_0 i})^2 \qquad (36)$$

is a minimum. In this calculation the zero-pressure extrapolated result for ν_0' $(=a)$, its standard deviation, the slope of the straight-line fit b, and its standard deviation are obtained. The standard deviation in a thus obtained represents the statistical error and is ± 0.411 MHz.

   b. Postulated modified Lorentzian line shape. The precision resonance data are obtained with sufficient power to quench 63% of the metastable α-state ions. Thus a true description of the line shape is given by expression (28), instead of expression (26) which was used in data processing. The matrix-element variation $C_{\alpha e}$ and the Zeeman curvature lower the Lamb-shift result in expression (26) more than they actually should [as in (28)]. The resulting correction for this effect is 2.328 ± 0.267 MHz (see Appendix C).

   c. Other quenching effects. In addition to obtaining results at three different operating helium-pressure values at the same quenching power level, data were also obtained under normal operating pressure at three different quenching power levels. If the power index η is defined as the ratio of the operating power level P to the characteristic power level P_0 [see expression (3)], then $\eta = 0.5$, 1, 2, and 3 correspond to quenching levels 35, 63, 84, and 95%, respectively, three of which correspond to the experimental quenching levels. The resonance line center values obtained at the different values of η as described in Appendix C are used for comparison with the experimentally observed resonance-center values (after corrections for the rf power-dependent systematics previously described are applied see Table II). The resonance-center value corresponding to $\eta = 1$ is taken as reference, with respect to which shifts in the resonance center $\nu_0(\nu_p)$ at other values of η are shown in Fig. 13. There is no evidence of any other quenching effects at low rf power levels up to around our normal operation value and hence no corrections are applied.

VIII. RESULTS AND DISCUSSION

Precision experimental results are based on 38 experimental runs, although additional runs were made to check on the filament bending and rf power-dependent effects. Eight runs were discarded because of apparatus malfunction. The runs are grouped according to the operating conditions of the apparatus and are recorded in Table I. The weighted mean values for the resonance center of the groups are recorded under the column $\nu_0 + \Delta\nu_0$, where weighting coefficients are the inverse squares of the standard deviations. The average value of group V (with displaced filament) agrees well with group III, giving no strong evidence of any significant filament bending effect.

The operating helium pressure is the variable in groups I– IV and these groups constitute precision results. These runs were fitted to a straight line by means of weighted least squares and constitute the precision resonance data. The zero-pressure extrapolated value for the resonance center thus obtained is
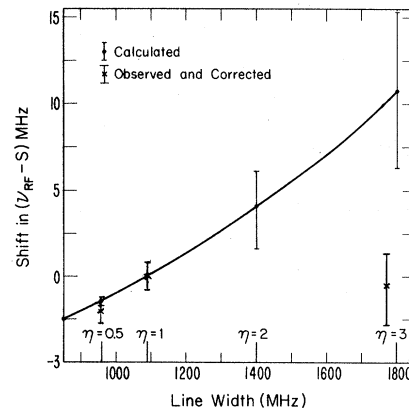

FIG. 13. Shift in the resonance center frequency $\nu_0'(\nu_p)$ $= \nu_{rf} - S$ as a function of the resonance linewidth (rf power). Observed resonance centers after all power corrections are made are shown.

TABLE III. Corrections and uncertainties to the Lamb shift (S) with 63% quenching power level (in MHz).

Effects intrinsic to the ion:	
Stark shift (Sec. VII A a)	0.004 ± 0.118
Overlap correction (Sec. VII A d)	0.096 ± 0.113
rf stark effect (Sec. VII A f)	-0.117 ± 0.058
Effects characteristic of ion assemblage:	
Field dependence of space-charge motion and collision quenching[a] (Sec. VII B c)	± 1.000
Deviations from ideal apparatus: (Sec. VII B c)	
Magnetic field inhomogeneity (Sec. VII C a)	-0.570 ± 0.025
rf power variation (Sec. VII C b)	-0.050 ± 0.050
Grid transmission variation (Sec. VII C c)	-0.250 ± 0.050
Detector gain variation (Sec. VII C d)	± 0.160
Field dependence of quantum convertor (Sec. VII C e)	-0.125 ± 0.125
Field effects on associated electronics (Sec. VII C g)	-0.125 ± 0.125
Corrections from method of analysis:	
Least-squares calculation: statistical error, one standard deviation (Sec. VII D a)	± 0.411
Data-processing method (Sec. VII D b)[a]	$+2.328 \pm 0.267$
Total correction and uncertainty with one standard deviation	$+1.191 \pm 1.214$
Total correction and uncertainty with three standard deviations	$+1.191 \pm 2.013$

[a]These two effects have correlated uncertainties.

$$\nu_0'(\nu_p) = \nu_{rf} - S = 15\,244.947 \text{ MHz} , \qquad (37)$$

where $\nu_{rf} = 29\,290.000$ MHz. The standard deviation in this result is ± 0.411 MHz (as described in Sec. VII D). The slope of the straight-line fit and the standard deviation of the slope are 0.108 and 0.081 MHz, respectively. This result would imply a correction of -0.497 ± 0.372 in S, if all the data were taken at a single pressure of 4.5 mTorr, with the error being one standard deviation. Sources of contribution for the pressure shift are discussed in Secs. VII B b, VII B c, and VII B e.

Groups IV, VI, and VII show the results with the quenching power level as a variable at the normal operating values for the other parameters. These results serve two purposes. First, we obtain normalization results from groups VI and VII, where the ratio signals are least-squares fitted to the ratio line-shape equation (29). Convergent results thus obtained are in group VIII and are used to provide a check on the precision results. Convergence refers to the least-squares-fit calculation resulting in physically meaningful parameters in less than 40 iterations in the computer program.

The second purpose of the groups IV, VI, and VII is to compare observed resonance center as a function of the rf power after the power-dependent corrections to $\nu_0'(\nu_p)$ as shown in Table II with calculated values.

The calculated normalized signal

$$Z(\nu_p) = I(\eta = 0.5)/I(\eta = 3)$$

when least-squares fitted to the ratio line-shape equation (29) gives a line center for the ratio signal

which is lower by 8.193 ± 0.686 MHz than the calculated $\eta = 1$ resonance center. The observed normalized result (Table I, group VIII) is obtained without applying any power-dependent corrections to the data with 35% Q and 95% Q and thus is lower only by 0.422 ± 1.650 MHz than the observed resonance center with 63% Q.

Table III shows all necessary corrections made to the zero-pressure extrapolated precision result for S ($2\,^2S_{1/2} - 2\,^2P_{1/2}$) obtained with 63% quenching power level. The final result for S with three standard deviations for the statistical error (1.233 MHz) plus systematics (1.191 ± 0.803 MHz) is

$$S(\text{He}^+)_{n=2} = 14\,046.2 \pm 2.0 \text{ MHz} , \qquad (38)$$

and the result with one standard deviation for the statistics is

$$S(\text{He}^+)_{n=2} = 14\,046.2 \pm 1.2 \text{ MHz} . \qquad (39)$$

This result agrees with all previous experimental results, except that of Lipworth and Novick,[7] whose value for S is $14\,040.2 \pm 4.5$ MHz with three standard deviations for the statistical error and hence the agreement is good within three standard deviations only. The most recent theoretical value for the Lamb shift is due to Applequist and Brodsky[21] and is

$$S(\text{He}^+)_{n=2} = 14\,044.5 \pm 5.2 \text{ MHz} . \qquad (40)$$

Thus our measured value for the Lamb shift in the $n = 2$ level of singly ionized helium represents agreement with theory.

APPENDIX A: ION-REMOVAL TIME FROM 63% Q POWER LEVEL AT NORMAL CONDITIONS

The probability per second of the induced transitions $\alpha \to e$ is given by Eq. (1). At the resonance center this is

$$\Gamma_\alpha = \frac{S_0}{h} \frac{e^2}{\hbar c} \frac{\Gamma_e^2 z_{\alpha e}^2}{\mu^2} , \tag{41}$$

where the symbols are defined in Sec. IV B.

If the input power to the Fabry-Perot resonator is p W and the Q of the resonator is Q_0, then the power available to induce the transition is pQ_0 W which is essentially distributed over the area of the spot size w,[22] so that the power per cm^2 is $2pQ_0/\pi w^2$. The power falls off at the edge of the spot size to about $\frac{6}{10}$ of its peak value at the center. The spot size is defined in terms of the field amplitude at the edge of the "spot." The amplitude at the edge is $1/e$ times the amplitude at the center. Taking this into consideration and the fact that the ion beam is close to the $x = 0$ plane, we have approximately

$$S_0 = \frac{10}{6} pQ_0 \times 10^7 \text{ erg/cm}^2 \text{sec}. \tag{42}$$

For 63% quenching at the normal operating conditions (see Fig. 11), $p = 0.75$ mW into the resonator. With $Q_0 = 1600$ for the resonator and spot size $w = 1.238$ cm, we have

$$S_0 = 25.0 \times 10^6 \text{ erg/cm}^2 \text{sec}. \tag{43}$$

Using Eq. (43) in Eq. (41), we get

$$\Gamma_\alpha = 97.6 \times 10^5/\text{sec} . \tag{44}$$

For 63% quenching, $\Gamma_\alpha \tau_\alpha = 1$, where τ_α is the ion removal time; thus we have

$$\tau_\alpha = 0.11 \text{ } \mu\text{sec}. \tag{45}$$

Assuming a 10% error in the p and Q values, we have

$$1/\tau_\alpha = (9.09 \times 10^6) \pm (0.91 \times 10^6)/\text{sec}.$$

APPENDIX B: MATRIX-ELEMENT VARIATION AND SIGNAL-LIGHT INTENSITY REDISTRIBUTION

The mixing of states with $m_j = \pm (l - \frac{1}{2})$ having same n and l but different j by the applied magnetic field makes the wave functions and energy levels of these states be magnetic field dependent. Bethe and Salpeter[9] give exact expressions for these wave functions for general field strength in the form of two-component Pauli spinors which can be used to calculate squares of matrix elements. Calculating $|\langle \alpha|z|e \rangle|^2$ at a general field H and relating it to the zero-field value, we can obtain $C_{\alpha e}$ as

$$C_{\alpha e} = \tfrac{3}{2}(1 - \delta_+), \tag{46}$$

where

$$\delta_+ = (\tfrac{1}{2} + \chi)(1 + \tfrac{2}{3}\chi + \chi^2)^{-1/2} \tag{47}$$

and χ is defined by Eq. (22).

If written as a function of H_p,

$$\delta_+ = \frac{\tfrac{1}{3} + \mu_B H/\Delta E}{[1 + \tfrac{2}{3}\mu_B H/\Delta E + (\mu_B H/\Delta E)^2]^{1/2}} . \tag{48}$$

The signal in the experiment is the flux of 304-Å photons emitted by the e-state decay to the ionic ground state characterized by $n = 1$, $l = 0$, $j = \frac{1}{2}$, and $m_j = \pm \frac{1}{2}$. If we label these two magnetic substates α' and β', the radiation in the observation direction x comes from the transitions $e \to \alpha'$ (with z polarization) and $e \to \beta'$ (with y polarization). The matrix elements involved are then $|\langle e|z|\alpha' \rangle|^2$ and $|\langle e|y|\beta' \rangle|^2$, and these are of equal magnitudes at zero magnetic field. Their variations with magnetic field can be calculated in a similar fashion to obtain

$$C_{e\alpha'} = \tfrac{3}{2}(1 - \delta_+), \tag{49}$$

$$C_{e\beta'} = \tfrac{3}{4}(1 + \delta_+). \tag{50}$$

The total effect is then

$$C_{eg} = \tfrac{1}{2}(C_{e\alpha'} + C_{e\beta'}) = \tfrac{9}{8}(1 - \tfrac{1}{3}\delta_+). \tag{51}$$

APPENDIX C: DATA-PROCESSING CORRECTION

The precision resonance data are taken with sufficient power to quench 63% of the available metastable ions. This would be all right if the observed signal levels at various magnetic field values are least-squares fitted to expression 28. The use of the low-power approximated expression (26) for the line shape yields resonance-center values different from (28) owing to the fact that the αe-matrix-element variation and Zeeman curvature occur in the exponential in (28). So it is necessary to calculate the differences in resonance-center values between expressions (26) and (28) at various power levels, not only to provide the data-processing correction but also in comparison of the observed and calculated line centers as a function of rf power (i.e.,

linewidth).

The calculation is done by starting with a theoretical line (center ν_0, width $\mu = 860$ MHz) described by (26) which is a Lorentzian line modified by $C_{\alpha e}$ and C_{eg} and is rewritten as

$$x(\nu_p) = I(\nu_p)/I_0 , \tag{52}$$

where I_0 is the maximum signal at the resonance center,

$$I_0 = KC_{\alpha e}(\nu_0')C_{eg}(\nu_0')/\mu^2. \tag{53}$$

K is defined by Eq. (20).

Equation (28) (high-power signals) is rearranged as

$$S'(\nu_p) = I(\nu_p)/I_0 = (1 - e^{-\eta x(\nu_p)})C_{eg}(\nu_p), \tag{54}$$

where η is the rf power index; $\eta = 0.5$, 1, 2, and 3 corresponds to 35, 63, 84, and 95% Q, respectively. At each of the η values, $I(\nu_p)$ is calculated so that it represents the actual observed signals at various magnetic field values. These calculated signals are then least-squares fitted to (26) which is similar to data from data processing. The line center obtained for $\eta = 1$ by this calculation is taken as reference, and deviations of other line centers for other values of η are plotted as a function of η (i.e., a percent of Q or linewidth) in Fig. 13.

This calculation gives a frequency difference of 2.504 MHz between $\eta = 1$ and $\eta \ll 1$, which is the data-processing correction in the precision resonance data. Since the calculation was based on a natural linewidth of 860 MHz instead of 800 MHz, necessary correction and estimated error are calculated to be 2.328 ± 0.267 MHz to s.

---

†Based upon work submitted by Musti A. Narasimham in partial fulfillment of the requirements for the degree of Doctor of Philosophy to the Department of Physics and Astrophysics, University of Colorado, Boulder, Colo.

*Work performed at and supported by Natl. Bur. Std., Boulder, Colo.

[1]The series of papers on experiments performed by Lamb and collaborators have been referred to in the literature as HI, HII, HIII, HIV, HV, and HVI. These are W. E. Lamb, Jr. and R. C. Retherford, Phys. Rev. 79, 549 (1950), referred to as HI; 81, 222 (1955), HII; W. E. Lamb, Jr., ibid. 85, 259 (1952), HIII; W. E. Lamb, Jr. and R. C. Retherford, ibid. 86, 1014 (1953), HIV; S. Triebwasser, E. S. Dayhoff, and W. E. Lamb, Jr., ibid. 89, 98 (1953), HV; E. S. Dayhoff, S. Triebwasser, and W. E. Lamb, Jr., ibid. 89, 106 (1953), HVI.

[2]R. T. Robiscoe, Phys. Rev. 138, A22 (1965); R. T. Robiscoe and B. L. Cosens, Phys. Rev. Letters 17, 69 (1966); R. T. Robiscoe, Phys. Rev. 168, 4 (1968).

[3]B. L. Cosens, Phys. Rev. 173, 49 (1968).

[4]W. E. Lamb, Jr. and Miriam Skinner, Phys. Rev. 78, 539 (1950).

[5]P. F. Yergin, Ph. D. thesis (Columbia University) (unpublished).

[6]R. Novick, E. Lipworth, and P. F. Yergin, Phys. Rev. 100, 1153 (1955).

[7]E. Lipworth and R. Novick, Phys. Rev. 108, 1434 (1957).

[8]J. Shapiro and G. Briet, Phys. Rev. 113, 179 (1959).

[9]H. Bethe and E. E. Salpeter, Quantum Mechanics of One- and Two-Electron Systems (Academic, New York, 1957); see also HIII.

[10]F. N. H. Robinson, J. Sci. Instr. 36, 481 (1959).

[11]F. S. Johnson, K. Watanabe, and R. Tousey, J. Opt. Soc. Am. 41, 702 (1951).

[12]R. Allison, J. Burns, and A. J. Tuzzolino, J. Opt. Soc. Am. 54, 747 (1964).

[13]E. C. Bruner, Jr., Ph. D. thesis (University of Colorado, 1964) (unpublished).

[14]See Ref. 4, p. 546.

[15]N. F. Mott and H. S. W. Massey, Theory of Atomic Collisions (Oxford U. P., London, 1959), p. 236.

[16]R. Helm, K. Spangenberg, and L. M. Field, Elec. Commun. 24, 1 (1947).

[17]D. T. Wilkinson and H. R. Crane, Phys. Rev. 130, 852 (1963).

[18]E. B. D. Lambe, Ph. D. thesis (Princeton University, 1959) (unpublished).

[19]E. Lipworth, Ph. D. thesis (Columbia University, 1955) (unpublished).

[20]Musti A. Narasimham, J. Opt. Soc. Am. 59, 781 (1969).

[21]T. Appelquist and S. J. Brodsky, Phys. Rev. Letters 24, 562 (1970).

[22]A. Yariv and J. P. Gordon, Proc. IEEE 51, 3 (1963).